JOURNAL OF GEOPHYSICAL RESEARCH, VOL. 106, NO. E10, PAGES 23,349–23,357, OCTOBER 25, 2001

Density structure of the upper thermosphere of Mars from measurements of air drag on the Mars Global Surveyor spacecraft

Philip W. Tracadas and Maria T. Zuber[1]

Department of Earth, Atmospheric and Planetary Sciences, Massachusetts Institute of Technology, Cambridge. Massachusetts, USA

David E. Smith and Frank G. Lemoine

Laboratory for Terrestrial Physics, NASA Goddard Space Flight Center, Greenbelt, Maryland, USA

Abstract. We present measurements of the density of the Martian atmosphere between 170- and 180-km altitude above the high northern latitudes over a 6-month period in 1998, when the solar cycle was beginning to rise out of its activity minimum. These measurements were made from the observed orbital decay of the Mars Global Surveyor (MGS) spacecraft during its Science Phasing Orbits (SPO) (April to September 1998) using X band Doppler tracking observations. The densities that we retrieve are comparable to model values given by *Culp and Stewart* [1984], *Stewart* [1987], Mars-GRAM 3.7 [*Justus et al.*, 1996], and recent Mars Thermospheric Global Circulation Model (MTGCM) simulations [*Bougher et al.*, 2000]. However, the SPO period can be divided into two time periods (separated at $L_S \approx 355°$~0°) that are characterized by significantly different orbit-to-orbit variability that is not predicted by these earlier models. The first time period corresponds to the time during which the MGS orbit perifocus moved toward the north pole while the local solar time was 1000–1100; during this period, orbit-to-orbit variability is 50–70%, and our average measured density at 175 km is 0.018 ± 0.007 kg km^{-3} (between 67° and 72°N and L_S=315° to 320°). The second time period corresponds to the time during which the orbit perifocus moved south from the north pole and the local time was 1700–1730; during this period, orbit-to-orbit variability is 40–20%, and our average measured density at 175 km is 0.024 ± 0.004 kg km^{-3} (between 62° and 69°N and L_S=17° to 28°). For both time periods the observed latitudinal gradient of density on a constant altitude surface exhibited a factor of 3–4 decrease between 60° and 90°N. This gradient is comparable to that expected by the polar vortex (high-latitude wind) effect modeled by the MTGCM for solar medium conditions at southern summer solstice [*Bougher et al.*, 2000]. A southern hemisphere dust storm that the MGS Thermal Emission Spectrometer (TES) observed at L_S=309° is distinguishable in our data set as a 100% rise in density at 180 km above the 70° northern latitudes 7 days later (L_S=313°).

1. Introduction

The use of atmospheric drag on the Mars Global Surveyor (MGS) spacecraft was a fundamental part of the mission plan for reaching the near-circular mapping orbit; however, the atmospheric drag effects on the spacecraft outside of aerobraking have so far been given little consideration beyond the engineering concerns of orbit maintenance. In this work we use measurements of drag on MGS to retrieve the density of the Martian atmosphere during the elliptical Science Phasing Orbit (SPO) mission phase. The atmospheric densities that we recover are at an altitude of 170–180 km (below the 400-km mapping orbits' yet above the aerobraking perifocus altitude range of 100–130 km). Spacecraft tracking and precision orbit determination have been used previously for density studies of Earth's upper atmosphere [*Walker*, 1979; *Boulton*, 1985], and in this study we modify and extend the technique to observe daily, weekly, and monthly changes in the density structure of the Martian thermosphere.

Different instruments on MGS are able to measure the density of the Martian atmosphere at a variety of altitudes using several independent observations and measurement techniques. The MGS radio science investigation [*Tyler et al.*, 1992] obtains observations from X band radio occultations of the neutral atmospheric density from 80-km altitude to the surface [*Hinson et al.*, 1999]. The Thermal Emission Spectrometer (TES) also probes the lower atmosphere below 50 km (nadir) and 75 km (limbscan) [*Christensen et al.*, 1998]. Wave 1, 2, and 3 structures have been detected from density measurements made between 110 and 170 km by the onboard spacecraft accelerometers during aerobraking orbits [*Keating et al.*, 1998; *Tolson et al.*, 1999]. The Martian neutral atmosphere is too tenuous above 230 km to be measured by any of the above techniques or other remote-sensing methods such as limb scanners and airglow.

[1]Also at Laboratory for Terrestrial Physics, NASA Goddard Space Flight Center, Greenbelt, Maryland, USA.

Paper number 2000JE001418.
0148-0227/01/2000JE001418$09.00

The Martian thermosphere (above 110 km) is not well sampled spatially or temporally. The Viking 1 and 2 and Mars Pathfinder landers each provided one vertical profile from accelerometer (and mass spectrometer, in the case of Viking) measurements during entry and descent under solar minimum conditions [*Nier and McElroy*, 1977; *Seiff and Kirk*, 1977; *Magalhães et al.*, 1999]. MGS accelerometer measurements have yielded over 1600 vertical profiles of atmospheric density [*Keating et al.*, 1999] while under solar minimum to medium conditions. The accelerometer measurements provide almost global sampling of the Martian thermosphere, but only below ~170-km altitude, and no data were obtained during SPO or over the north polar region or during solar maximum conditions (i.e., postaerobraking). However, Doppler tracking can be used to measure the orbital decay due to drag, and hence air density, during SPO and the long-term MGS mapping mission. These density measurements yield the response of the upper thermosphere (at 175 km and ~400 km) to solar ultraviolet (UV), extreme UV (EUV), and X-ray absorption heating and molecular thermal conduction cooling [*Bougher et al.*, 2000]. In addition, these upper atmosphere density measurements are sensitive to the expansion and contraction of the lower atmosphere (below 100 km). The heating and cooling in the lower atmosphere vary owing to changes in solar infrared flux (changes with the Mars–Sun distance and evolving solar cycle) and suspended dust (changes with the seasons) as well as various dynamic wave and tide effects. These measurements, made under solar medium to maximum conditions, can be used to validate models of Mars' thermospheric heating and dynamics, such as the Mars Thermospheric Global Circulation Model (MTGCM) [*Bougher et al.*, 2000].

The SPO mission phase of MGS consisted of 370 orbits characterized by a 167- to 174-km perifocus altitude (Table 1). During SPO there was little orbital maneuvering, and MGS experienced variable drag that reduced the spacecraft's orbital semimajor axis by 50 m on average for each orbit. Whereas the accelerometers are insensitive to the small, instantaneous drag force imparted by the very tenuous atmosphere at altitudes above ~170 km, the average air drag deceleration for an entire orbit revolution can be measured using an orbit-period time-variation method. This method and our orbit solution method are explained in detail herein. In the following sections we first present the tracking data and orbit solution method used to reconstruct the decaying orbits of MGS. We then calculate the atmospheric mass density near perifocus implied by this orbital decay. We conclude with analysis of the spatial and temporal patterns of the thermospheric density during the SPO time period (northern winter and spring) and a comparison to density predictions from pre-MGS models.

2. Data and Orbit Determination

During the SPO orbits, the MGS spacecraft was tracked by several radio antennae in the NASA JPL Deep Space Network (DSN). The X Band tracking data consist of one-way constant frequency and two-way and three-way ramped frequency Doppler as well as two-way ramped range measurements that utilized both the high- and low-gain antennae on board MGS. To improve the ability to achieve and maintain lock, the Doppler signal is "ramped," i.e., uses continuous linearly increasing and decreasing, instead of constant, oscillator frequencies [*Moyer*, 1973; *Moyer*, 1987]. Owing to pointing restrictions of the MGS antennae and DSN lock-on delay when establishing two- or three-way tracking, one-way Doppler observations were received from an MGS low-gain antenna during perifocus passage, and two- and three-way Doppler and two-way range were established using the MGS high-gain antenna during the rest of the orbit [*Lemoine et al.*, 1999a]. Overall, tracking data quality is excellent with the worst tracking type (one-way Doppler) yielding a 0.03 mm s^{-1} accuracy averaged over 10 s (R. Simpson, personal communication, 2001).

For 4 weeks during SPO, Mars and Earth were near solar conjunction, and no useful tracking data were obtained during this time. Thus our data span the periods from the end of the aerobraking 1 period (March 27, 1998) to the beginning of the solar conjunction command moratorium interval (CMI) (May 1, 1998) and from the end of solar conjunction CMI to 6 days before the aerobraking 2 period (May 28 to September 17, 1998). During this time the north hemisphere of Mars was entering spring as Mars moved from L_S=300° to L_S=30°. L_S is the areocentric longitude of the Sun and is a measure of the Martian seasons: L_S=0°, 180° are the equinoxes, and L_S=90°, 270° are the northern summer and winter solstices, respectively.

To process the Doppler tracking data, we utilized the GEODYN batch least squares orbit determination program [*Pavlis et al.*, 2001]. The orbit solution method is detailed by *Lemoine et al.* [1999b]. Here we have used the same data, ephemerides, and force models as they did, with the exception of a new gravity model (MGM0989a), which is a more recent 70 degree and order spherical harmonic model that incorporates more MGS mapping-orbit tracking [*Lemoine et al.*, this issue]. We processed the spacecraft tracking data in arcs of eight to ten orbits (4–5 days).

In brief, the orbit modeling included a Mars gravity field model (MGM0989a), third body perturbations due to the Martian moons, the Sun, and planets, and nonconservative forces such as atmospheric drag, solar radiation pressure, and the pressure of infrared radiation emitted from Mars. We constructed a ten-plate macromodel from the MGS blueprints to compute the nonconservative forces. We also used the telemetry quaternions to define the spacecraft attitude and solar array orientation. At each time step in the orbit integration, we computed the nonconservative forces incident on each plate and summed the forces vectorially to compute the total nonconservative force acting on the satellite. The Mars radiation pressure model is based on Viking infrared thermal mapper (IRTM) data [*Kieffer et al.*, 1977; *Lemoine*, 1992] and includes reflected solar radiation due to the planet's albedo as well as the planet's thermal emission. The Mars radiation pressure ranges in amplitude from 1% to 30% of the direct solar radiation effect, peaking in the vicinity of the subsolar point and reaching minima when the spacecraft passes over the poles. The *Stewart* [1987] atmospheric density model was used in the atmospheric drag computations. To best fit the orbit model to the tracking data, we solved for a linear scaling coefficient that modulates the magnitude of the drag force. The drag perturbation peaked at 10% of the amplitude of the direct solar radiation pressure perturbation but varied with spacecraft altitude and spacecraft cross-sectional area projected in the along-track direction. The resulting orbit solutions yielded root mean square (RMS) fits to the tracking data of 0.3 mm s^{-1} for one-way Doppler, 0.2 mm s^{-1} for two- and three-way Doppler, and 40 m for two-way range.

The orbit of MGS during SPO is highly eccentric (e = 0.7) with an average period of 11.64 hours, a perifocus altitude be-

Table 1. Orbit Model Parameters and Average Elements

Model parameters and orbit elements	Value
Total tracking measurements	188,973
Gravity field	MGM0989a (70 x 70)
GM	42,828.372 $km^3 s^{-2}$
Semimajor axis (average)	12,396 km
Eccentricity (average)	0.7135
Inclination (average)	93.76°
Argument of perifocus[a]	118° – 60°
Longitude of the ascending node[a]	323° – 331°
Orbital period (average)	11.64 hours

[a]Values at the beginning and end of SPO. Each element monotonically traversed its range.

tween 167 and 174 km, and an orientation and precession that moved the perifocus from 61°N to 86.3°N and back to 60°N (see Table 1 for further details).

The orbit evolution due to drag is best presented by plotting the semimajor axes of the MGS SPO orbits over time. Figure 1a shows the osculating semimajor axis of each orbit at apofocus from the beginning of the MGS mission (orbit insertion) to the end of the aerobraking 2 mission phase (just prior to entry into the 400-km circular mapping orbit). Figure 1b shows the SPO period enlarged. The average semimajor axis decay during SPO was 50 m $orbit^{-1}$ during aerobraking, when the perifocus altitude was between 100 and 130 km; the decay range was 50–150 km $orbit^{-1}$ during the aerobraking 1 phase and 10–50 km $orbit^{-1}$ during the aerobraking 2 phase.

The SPO orbits (Figure 1b) show both the short-wavelength (9-sol, 9.2-day, 19-orbit) gravity perturbations due to the resonance effect of the even ordered terms of the Martian gravity field [*Lemoine*, 1992] and the long-wavelength decay due to atmospheric drag. The two-slope character of the drag (the beginning and end of SPO have a higher decay rate than the middle) is mainly due to the precession of the orbit perifocus over the northern polar region. Since Mars is flattened due to its rotation and the presence of the Tharsis bulge near the equator, the areoid (Martian equipotential surface) decreases in radius from the equator to the poles. Thus the MGS orbit perifocus effectively goes up and down in altitude by 4 km, i.e., of order a half to a third of a scale height, because of precession over the polar regions (Figure 2). The orbit perifocus radius also increases by 2.5 km during the first half of SPO owing to long-period gravity perturbations and reaches a mean level that is maintained during the second half of SPO. The combined altitude increase reduced the drag and resulted in a lower decay rate during the middle of SPO, while the later part of SPO showed a higher decay rate due to the increased drag caused primarily by the decrease in altitude above the areoid.

The quality of the orbit models can be quantified in three ways that are summarized in Table 2. The RMS difference in position between the overlap of contiguous orbit solution arcs gauges the consistency of the included orbit solution model components. We analyzed 12-hour overlaps at the beginning and end of each arc for 25 arcs. For all of SPO the RMS difference in position of these overlaps was 20 m in the radial direction, 155 m cross-track, and 330 m along-track, yielding a total position difference of 365 m. Similarly, the RMS overlap of the semimajor axis osculating orbit elements at apofocus from this study is 19 m. Altimetry from the Mars Orbiter Laser Altimeter (MOLA) [*Smith et al.*, 1999] provided an independent error check on the orbit position through perifocus [*Neumann et al.*, this issue]. The residual at perifocus between topography measurements made during SPO (with crossover correction) and the gridded MOLA topography collected during the mapping orbit yielded a RMS areocentric radius difference of 8.4 m for the 183 SPO orbits that incorporated MOLA data taken in nadir-pointing mode (G. Neumann, personal communication, 2000). We assume this value to be the error in the perifocus distance. Using the largest of these radial errors and Kepler's third law, we obtained a limit on the individual orbit period timing of 0.10 s.

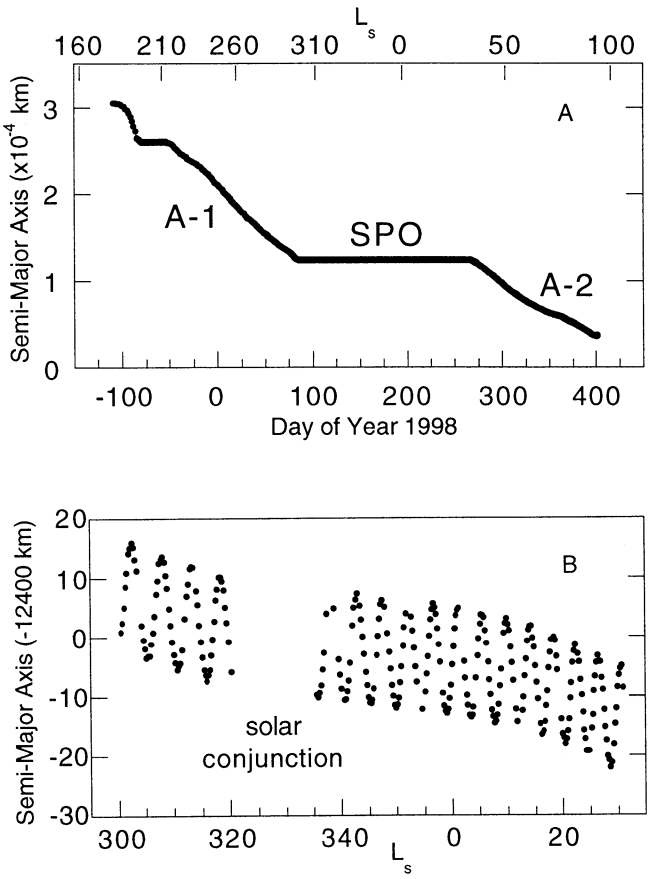

Figure 1. The evolution of the orbit of Mars Global Surveyor (MGS), shown as the orbital semimajor axis measured at each apofocus. (a) Evolution for the entire period before insertion into the mapping orbit. The average decrease in semimajor axis ranges from 150 km $orbit^{-1}$ at the beginning of aerobraking 1 to 10 km $orbit^{-1}$ at the end of aerobraking 2. During the Science Phasing Orbit (SPO) period the average decrease is 50 m $orbit^{-1}$. Orbit solution data are from the Mars Surveyor Operations Program (http://mars.jpl.nasa.gov/mgs/status/nav/navhist.html). L_s is areocentric longitude of the Sun, where L_s=0° is the beginning of northern spring. (b) Evolution during SPO only. Each point shows our orbit measurement using available tracking data with anomalous orbits for our analysis removed. The error in the length is at most 20 m. Notice the 9-sol 30-km variation caused by the even (longitudinal) terms of the Martian gravity field. A longer-wavelength monotonic decrease in the axis length (with a two slope character) is also evident and due to air drag (see text).

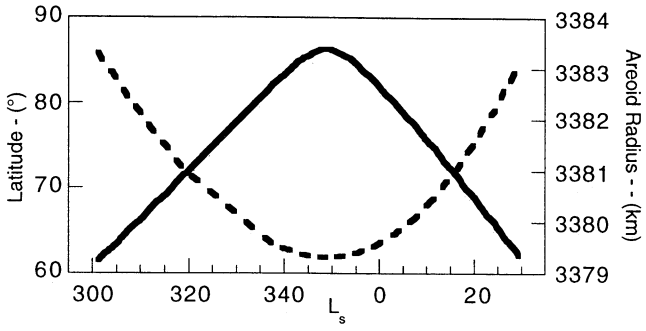

Figure 2. Perifocus latitude evolution during SPO and areoid radius. The spacecraft orbit perifocus precessed over the north polar region during SPO, resulting in perifocus latitude evolution (solid line). The radius of the areoid (3397-km mean equatorial radius) at the perifocus subspacecraft point (dashed line) varied owing to the combination of this precession and areoid flattening. The effective altitude of the spacecraft perifocus thus raised and lowered by 4 km during SPO because of this "bottom drop" effect.

3. Density Calculation

From the orbit solutions of MGS we derived the changes for each orbital period and applied orbit evolution theory to determine the mass density of the Martian thermosphere around 175-km altitude. This approach to calculating density is largely independent of the method used to solve for the orbit of MGS and was used mainly because at the inception of this work, these same orbits were also being used for gravity field estimation. To first order the gravity field is sensitive to the perifocus and nodal precessions, but at higher orders it is more sensitive to a and e and thus, for the densities encountered, would make the orbit solver less sensitive for drag estimation.

3.1. Problem Formulation

The theory for spacecraft orbit evolution in an atmosphere provides an expression for the change in the orbital period due to drag experienced within a few scale heights of orbit perifocus. The drag estimate has three components: (1) an exponential atmosphere given by the ambient air density $\rho(r)$ and a scale height H; (2) spacecraft-dependent drag parameters of size, mass, and drag coefficient; and (3) the characteristics of the orbit of the spacecraft that yield the velocity (for the aerodynamic drag component) and the amount of atmosphere traversed. Therefore, from measuring the change in orbital period due to atmospheric drag and assuming a scale height, it is possible to infer an atmospheric density. However, this measurement approach can be particularly sensitive to errors in H. The scale height is not accurately known in this part of the Martian atmosphere and probably varies from day to day. Therefore we adopt the approach of King-Hele and collaborators and evaluate the density at a height $0.5\,H$ above perifocus, where it is insensitive to changes in H. In this formulation a 25(50)% change in H produces a 1(3)% change in density. For a high-eccentricity ($e > 0.2$) orbit in an oblate atmosphere with day-to-night variation and a scale height H that varies linearly with altitude, the density (ρ_A) at $0.5\,H^*$ above perifocus is given by [*King-Hele*, 1987, equation (10.23), p. 188]

$$\rho_A = -\frac{(0.605-0.15\mu)\dot{T}}{\delta\sqrt{aH^*}}\left\{\Xi(e)+\frac{0.133KH}{a\sqrt{e}} +\frac{0.266\varepsilon}{\sqrt{e}}\sin^2 i\cos 2\omega\right\}\{1+O(\Psi')\}, \quad (1)$$

where μ is the rate of increase of H with height (not more than 0.2), H^* is our estimate of the scale height at perifocus to within 25% of the true H, δ is the spacecraft parameter (described below), $\Xi(e)$ is given by equation (2), K is the day-to-night variation, a is semimajor axis length (initial, e.g., we use the apofocus elements that precede the perifocus drag pass as an approximation of the mean orbit), e is initial eccentricity, ε is ellipticity of the atmosphere (assumed to follow the areoid), i is initial inclination, ω is the initial argument of perifocus, and the discarded higher-order terms are of order 0.001. The parameter $\Xi(e)$ for the high-eccentricity case is given by [*King-Hele*, 1987, equation (10.24), p. 188]

$$\Xi(e) = \frac{1}{3}\sqrt{\left(\frac{2e}{\pi}\right)}\left[\frac{(1-e)^{1/2}}{(1+e)^{3/2}}\left\{1+\frac{H(8e-3e^2-1)}{8r_p e(1+e)}\right\}\right] \quad e > 0.2, \quad (2)$$

where r_p is the radius at perifocus. The error (standard deviation) in the air density is usually <1% for reasonably accurate estimates of δ and H^*. For a high-eccentricity orbit, such as those during SPO, the effect of an oblate atmosphere is small and is represented by the geometric ε/e term, which has a range of –0.001 to –0.002 because of the evolution of the argument of perifocus during SPO. The day-to-night factor K is set to zero for the SPO period for two reasons: (1) the orbits precessed over the polar region where there is little effect from the solar bulge in the equatorial region near the subsolar point (more accurately, the perifocus region of the orbits was always >80° angular distance from the center of a presumed daytime bulge in the atmosphere having a center at the subsolar latitude and at 1400 local time in longitude), and (2) a bulge has not been observed in this part of the Martian atmosphere (although observed by TES observations at lower altitudes [*Conrath et al.*, 2000]), but using Earth-like parameters for a similar geometry, the predicted factor is small. The spacecraft parameter included in the aerodynamic drag equation is given by $\delta = FSC_D/m$ [*King-Hele*, 1987, equation (4.2), p. 44], where F is a factor for atmospheric rotation (assuming the rotation is the same as the planet, F is ~1.0073 during SPO [*King-Hele*, 1987, equation (2.23), p. 31]), S is the cross-sectional area of MGS perpendicular to the direction of motion (RMS area is 16.2 m^2 during SPO but is adjusted every orbit according to spacecraft quaternions), C_D is the drag coefficient (~2.13, as-

Table 2. Orbit Quality

Metric[a]	Value, m
RMS overlap of semimajor axis orbit elements at apofocus	19
RMS overlap of radial positions	20
RMS overlap of cross-track positions	155
RMS overlap of along-track positions	330
RMS overlap of MOLA-determined topography between SPO and Mapping at perifocus	8.4

[a]See section 2 for an explanation of each metric.

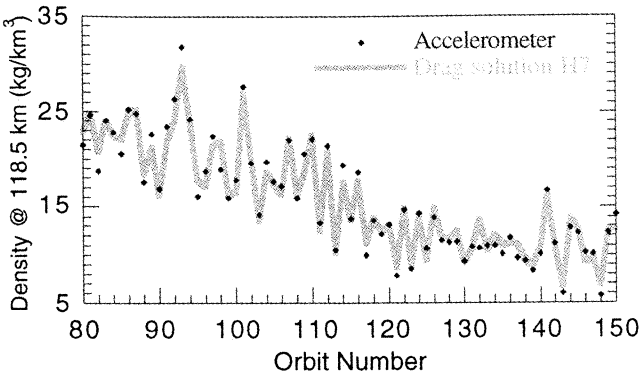

Figure 3. Comparison of density measurements made at 118.5-km altitude by two different techniques. The accelerometer measurements are from the Accelerometer Team (http://mars.jpl.nasa.gov/mgs/confrm/aerobexp.html, Figure 3). The drag solution uses orbit solutions from the Mars Surveyor Operations Program (http://mars.jpl.nasa.gov/mgs/status/nav/navhist.html), assumes the accelerometer-derived scale height of 7 km, uses appropriate aerobraking 1 parameters for δ [from *Esposito et al.*, 1998], and fits a coefficient of drag of 1.95. Note that the altitudes of the accelerometer measurements have been recalculated using the Goddard areoid (MGM0989a), resulting in a ~3.5-km decrease relative to their original presentation altitude.

suming free-molecular flow [*Wilmoth et al.*, 1999]), and m is the mass of MGS (760.4 kg at the beginning of SPO).

We use the pre-SPO aerobraking 1 orbits (History of Orbital Parameters, Mars Surveyor Operations Program, http://mars.jpl.nasa.gov/mgs/status/nav/navhist.html) to check and hone our density determination method because the long-wavelength orbital perturbations due to the gravity field of Mars are small compared to the large orbit changes due to aerobraking (100- to 150-km average reduction of the semimajor axis per orbit during aerobraking 1). Therefore we calculate the density using simply the difference in period between successive orbits. Figure 3 shows the general agreement between our method and the accelerometer data after adjustment of δ (including adjustment of the coefficient of drag to 1.95, which is very nearly the predicted C_D for MGS at the perifocus densities encountered during aerobraking [*Wilmoth et al.*, 1999]).

3.2. Orbital Period Measurement

The measurement of the change in orbital period must be corrected for the gravity perturbations that torque the MGS orbit during each perifocus passage. As shown in Figure 1b, the plot of orbital period is proportional to a by Kepler's third law and thus shows these same periodic oscillations. We remove these perturbations by numerically integrating each orbit for MGS from apofocus to subsequent apofocus (a "synthetic" orbit) about an airless Mars. These synthetic orbits include all solar and albedo radiation model parameters estimated in the original orbit solution and use the initial conditions of position and velocity of the spacecraft at each apofocus given by the orbit solution. Each synthetic orbit contains the gravity and radiation perturbations from which we subtract the observed orbit and derive the semimajor axis change due to the drag perturbation. Figure 4 shows the decrease in period for each orbit in SPO with good tracking data. We define "good" as at least several hundred tracking observations spanning the entire orbit. Additionally, we removed 17 orbits with thruster firings for angular momentum desaturation maneuvers. The general signature of drag during SPO described in section 2 is again evident in the inverted U shape of Figure 4; larger period reduction (higher drag) characterizes the beginning and end of SPO.

3.3. Density Structure Calculation

We initially assume a variety of scale heights in the range of 5–13 km and solve for the density at a half scale height above perifocus. *Esposito et al.* [1998] found an average scale height of 9 km in the 110- to 170-km range during aerobraking, while Viking 1 and 2 upper atmosphere mass spectrometer (UAMS) data yield scale heights of 11.7 and 6.7 km, respectively, between 165- and 180-km altitude. Because of the limited altitude range of our SPO dataset and systematic effects from the large L_S and latitudinal sampling, we were unable to derive a viable scale height from these data alone, so we adopted the *Esposito et al.* [1998] result of 9 km for our density estimate. Our $H^* = 9$ km solution is plotted in Figure 5a; the general structure and conclusions do not change appreciably for other reasonable ($H < 20$ km) scale heights.

Our measurements, plotted in Figure 5b with all available measurements of the Martian thermosphere above 110-km altitude, are bracketed by the Viking lander 1 and 2 late afternoon profiles [*Seiff and Kirk*, 1977]. Our derived density measurements are consistent with density measurements made at the beginning of SPO from orbit solutions by *Esposito et al.* [1998]. Figure 5b also confirms our assumption of a scale height of ~9 km as being reasonable.

4. Discussion and Conclusions

4.1. Observed Thermospheric Features During SPO

The evolution of the SPO thermosphere between 167 km and several scale heights above, where MGS experiences practically all of the air drag during an orbit, is best viewed by scaling our measurements to a common altitude (180 km) using a single scale height (9 km). This approach shows the true relative density variability from orbit to orbit. The relative

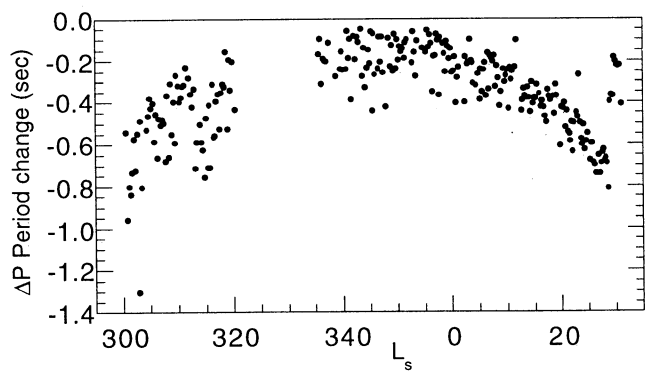

Figure 4. Orbit period decrease for each studied orbit during SPO. The inverted U shape is consistent with the variable drag partly due to orbit perifocus precession over the north polar region (see text). Smaller changes in the period at L_S~30° and other obvious small ΔP outliers are due to spacecraft maneuvering where the area in the direction of motion decreased substantially.

variability is insensitive to errors in the spacecraft parameters, although the absolute density values at 180 km for all orbits might be influenced because of these same errors.

Figure 6 shows the time evolution of the northern hemisphere thermospheric density. The minimum density is coincident with the period between the change of Martian season (northern spring equinox, L_S=0°) and the farthest northern perifocus passage of MGS (L_S=348°). The observed U pattern is not an artifact of misscaled densities, since a scale height <4 km (smaller than what the Accelerometer Team found at lower altitudes) would be needed to flatten the profile. The

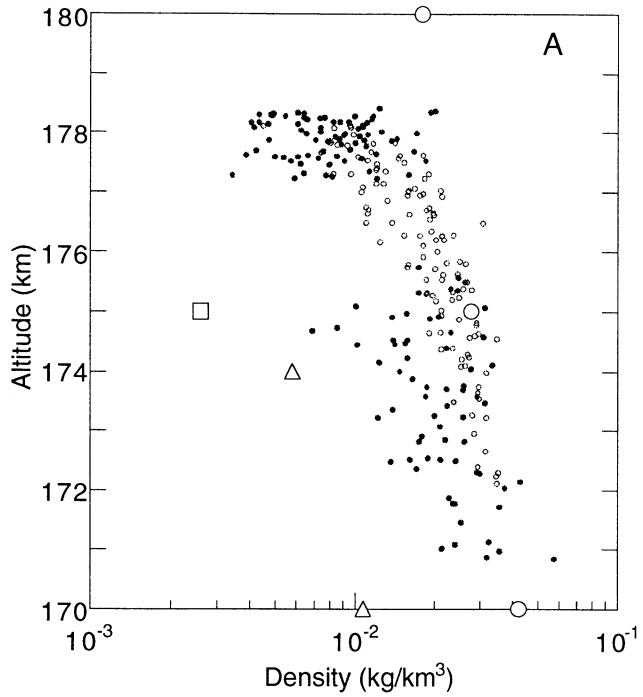

Tracadas *et al.* Figure 5a.

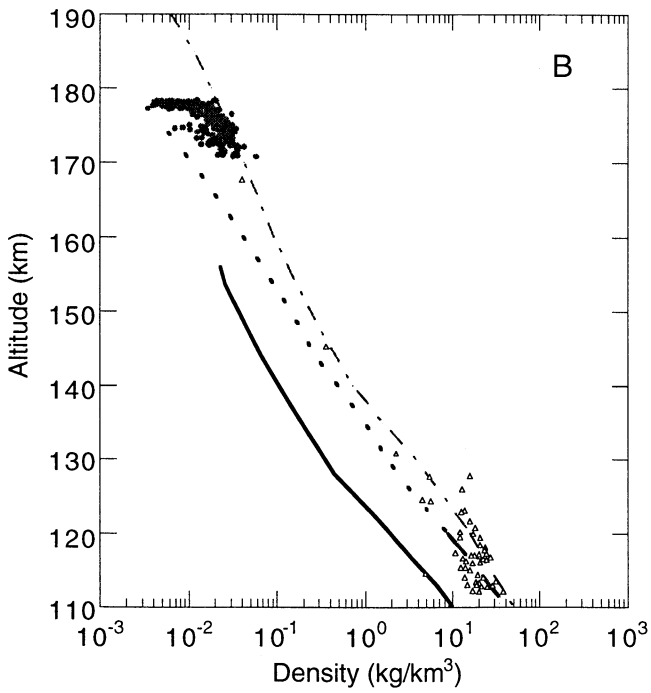

Bougher et al. [2000] MTGCM predicts a pattern similar to our observations and is discussed in section 4.2. The pattern is also asymmetric in two ways: first, the magnitudes of the rate of change differ (1) in density versus L_S (Figure 6) before and after the equinox and (2) in latitude (see Figure 8) before and after MGS's perifocus reaches its northernmost point (L_S=348°); second, the orbit-to-orbit variability before L_S≈355°~0° is 50–70% and 40–20% after (decreasing with time). These asymmetries may be due to differing local solar time regimes of the orbit perifocus about L_S=348°. Before L_S=348° the local solar time is around 1000–1100, while after L_S=348° the local solar time evolves to sunset evening hours (1700–1730). Martian orbital eccentricity effects are more gradual. The Martian perihelion occurs at L_S=251°, and the aphelion occurs at L_S=71°. Therefore, during SPO a general shrinking of the entire atmosphere is expected (about -6×10^{-5} kg km^{-3} per degree of areocentric longitude at 180 km) as distance to the Sun increases (i.e., the solar flux decreases). However, this does not explain either of the observed asymmetry features.

The density of the Martian atmosphere at 180-km altitude increases by 100%, indicating a heating and expansion of the lower atmosphere starting at L_S=313° and continuing to at least L_S=320°. Solar conjunction blocked observation of the full decay of this event. The event may be a delayed reaction to a southern hemisphere regional dust storm observed north and west of the Argyre impact basin at L_S=309°–319° [*Clancy et al.*, 2000; *Smith et al.*, 2000]. *Smith et al.* [2000] found that storm was nearly as intense as the Noachis storm, which was well observed in the aerobraking 1 accelerometer data as a 130% density increase at 110 km, but the Noachis dust storm was much more confined spatially. The average dust optical depth in TES observations from 15° to 30°N (their northernmost observations) increased from 0.1 to 0.35 from L_S=310°–315° [*Smith et al.*, 2000, Plate 1] compared to an increase of 0.35 to 0.75 for the Noachis storm. *Smith et al.* [2000] also observed a few isolated local dust storms in the northern hemisphere unrelated to this southern regional storm at the same time. Other local dust storms observed by the TES instrument at L_S=304°, 0°, 3° [*Smith et al.*, 2000] and a storm observed with Earth-based millimeter-wavelength observations at L_S=340° [*Clancy et al.*, 2000] show subtle evidence of their heating effect beyond the variability of our data series. Therefore the L_S=313° event is probably related to the Argyre storm.

Figure 5. Measured density structure of the Martian thermosphere. (a) Measurements made by the period-timing technique in this paper assuming a 9-km scale height. Solid circles are measurements before L_S=0°, and small open circles are measurements thereafter. The error in the altitude position is meter level, and the error in the densities is on order 0.005 kg km^{-3}. Other measurements are Viking 1 upper atmosphere mass spectrometer (UAMS) data (large open circles), Viking 2 UAMS data (triangles), and Pathfinder's top measurement extrapolated to 175 km using a 9-km scale height (square). (b) All available density measurements of the Martian atmosphere above 110-km altitude. Viking measurements (VL1=dash dot, VL2=dotted line) from *Seiff and Kirk* [1977], Pathfinder Atmospheric Structure Instrument (ASI) measurements (solid line, rereferenced in altitude to the MGM0989a areoid) from *Magalhães et al.* [1999], JPL navigation measurements (open triangles) from *Esposito et al.* [1998].

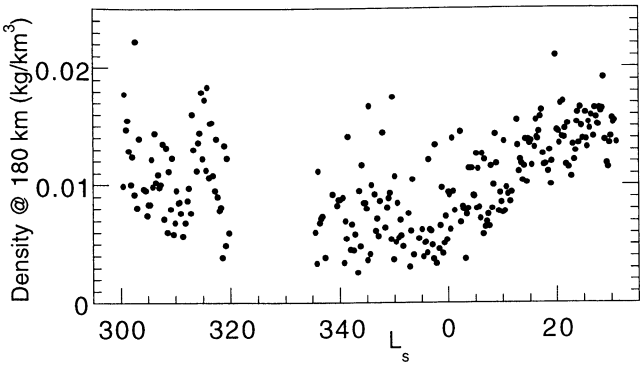

Figure 6. Time evolution of the northern hemisphere Martian thermosphere. All density measurements scaled to 180 km assuming a 9-km scale height are plotted as dots. See text for an explanation of features.

Following the lead of the Accelerometer Team, which found diurnal density wave 1 and 2 activity at lower altitudes [*Keating et al.*, 1998], we show in Figure 7 density versus longitude at two different local solar time ranges. Figure 7a is for the range of perifocus local times between 1000 and 1100 (during the first part of SPO ending at L_S=348°), and Figure 7b is for the second part of SPO, when the local times clustered around 1700–1730. There appears to be no detectable long-term, wave-like structure over the polar latitudes at 180-km altitude. Wave activity is expected to be negligible because of the altitude (many scale heights above the region where breaking gravity waves deposit their energy) and polar season (diurnal density waves are low amplitude in the polar winter season). However, Figure 7c shows the longitudinal dependence of density during the decay of the L_S=313° event and reveals a wave 1 type structure. If the lower atmosphere heating event that caused the increase in thermospheric density were situated at the longitude of the wave 1 maximum, then the Argyre storm (~300°E) is a poor match, but since the storm location was south of the equator, atmospheric circulation combined with the concurrent local storms in the north might explain the phenomenon. No other time periods during SPO show clear longitudinal structure.

4.2. Comparison With Density Models

Previous models of the Martian atmosphere are based on a variety of atmospheric measurements from the Mariner and Viking eras. Since there were no density measurements taken of the polar thermosphere before MGS, global circulation models using pre-MOLA topography or hydrostatic chemical mixing models are the basis for the available pre-MGS density models of the polar thermosphere. Plate 1 shows the comparison between our results and several thermospheric models.

Both *Culp and Stewart* [1984] and *Stewart* [1987] were designed to estimate global mean conditions and are of the hydrostatic chemical mixing model family. These models do not produce realistic variations with latitude and hence overestimate the "dust storm season" (L_S≈160°–330°) heating effect in the polar regions by an order of magnitude (see Plate 1). After the full decay of the dust functions in these models (by L_S=0°) and the progression of MGS perifoci toward equatorial latitudes, the *Stewart* [1987] model with incorporation of Earth-observed solar flux comes into good agreement with our observations.

The Mars-GRAM model 3.7 [*Justus et al.*, 1996] revised the *Stewart* [1987] model by tuning it for latitude, subsolar latitude, time-of-day, and other climate variations with output from the MTGCM circa pre-MGS [*Bougher et al.*, 1990, 1993]. We ran the model using the default settings, no climate factors, and the model's predicted solar flux. The phase of the Mars-GRAM model matches our data well, but the model underestimates our measurements until L_S>20°. Mars-GRAM 2000 and 2001 use this same revised Stewart-type model for altitudes above 170 km.

Latitudinal variations with season and solar time are the most valuable results of this study for thermospheric modelers.

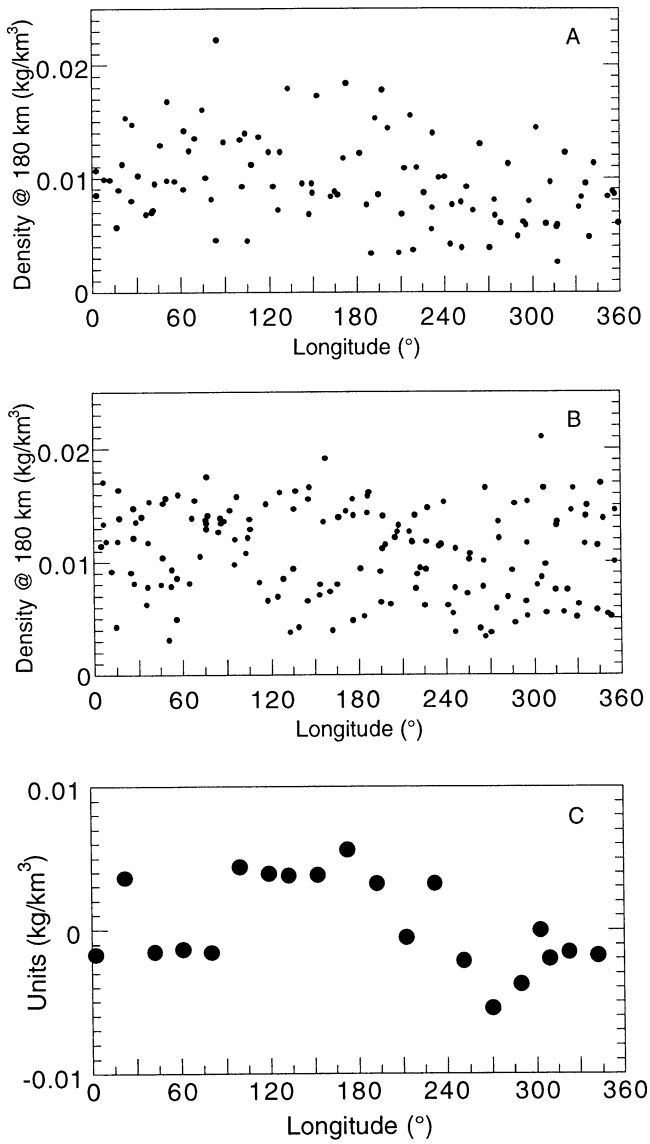

Figure 7. Density at 180 km versus east longitude separated by L_S=348°. Density scaling is the same as Figure 6. All measurements are (a) before and (b) after L_S=348°. (c) Longitudinal variation during the decay of the heating event that started at L_S=313°. A linear trend has been fit and removed from the event's decay (L_S=314°–320°), and the residual has been plotted versus longitude. The time series begins at longitude 302° and increases by 190° for each subsequent data point. The latitude spanned is 69°–72°N. See text for discussion.

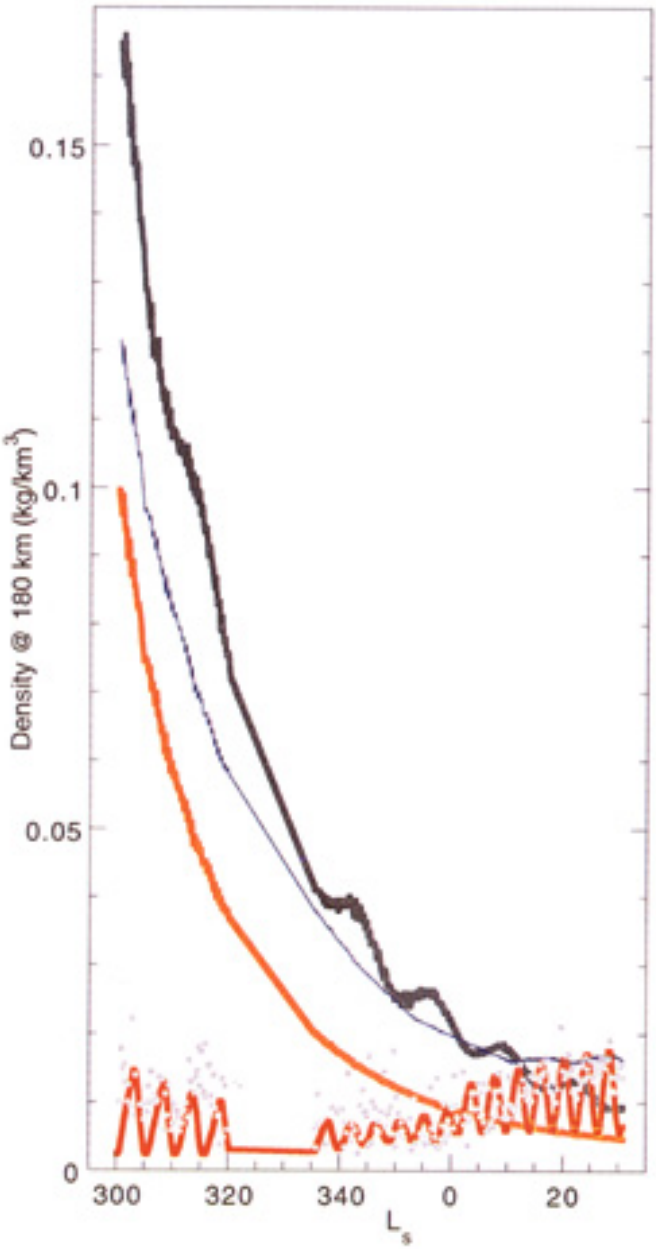

Plate 1. Density predictions from three models. *Culp and Stewart* [1984] (dark gray), *Stewart* [1987] model using model-predicted solar flux (orange) and actual 81-day averaged flux (blue), and Mars-GRAM 3.7 [*Justus et al.*, 1996] (red). Our measurements are plotted in gray for comparison.

As MGS's perifocus moved north (dots in Figure 8), the density at a given altitude (180 km) decreased by a factor of 3–4 between 60° and 86°N (Mars' position and season also evolved, L_S=300°–348°). As MGS's perifocus moved south over the same latitude range (circles in Figure 8) during northern spring, the density at the given altitude increased (a factor of 4, see Figure 6 also) and is consistently less variable and higher valued than the north-going density profile. Evolving northern spring, changes in local time, and/or the edge of a north moving solar bulge might be contributing factors to the slightly higher valued profile, but the general shape match with the early SPO profile suggests that a circulation pattern is maintaining the profile. Strong polar "vortex" wind zones have been modeled in the MTGCM during the solstices under varying solar fluxes and are shown to encircle the pole starting about ±60° latitude [*Bougher et al.*, 2000]. These winds have horizontal velocities of 200–300 m s^{-1} near the exobase, and the density profile implied by these winds has been recently modeled by *Bougher et al.* [2000] under "nondusty" atmospheric conditions with a revised MTGCM tuned with thermospheric density data from the MGS accelerometer.

Our observed latitudinal density gradient of a factor of 3–4 over 60° to 90°N at 180 km during equinox is comparable to that predicted by the MTGCM for southern summer solstice, solar medium, nondusty conditions with high-latitude winds (Figure 8). At the beginning of SPO, which is soonest after the southern summer solstice (L_S=270°), the local solar time of the observations is ~7 hours before the model's local time, yet the model overestimates the general density despite the nondusty conditions in the model. As MGS perifoci reach their northernmost point in the middle of SPO, the model and measured densities are in good agreement, but after the local time of our measurements changes to early evening and particularly after the equinox, the model consistently underestimates our measurements despite the smaller Mars–Sun distance in the model. Further thermospheric modeling and observations that focus on winds in the Martian polar regions are necessary to understand conditions between the solstices and during the solar cycle.

4.3. Future Work

These density measurements pave the way for verifying extracted measurements of Martian atmospheric density made with the GEODYN batch least squares orbit determination program. Once calibrated with these SPO measurements, we will be able to measure density changes during the mapping orbits at 400-km altitude despite the continual spacecraft maneuvering and frequent thrusting. Thus monitoring of the density structure of the Martian thermosphere and its temporal variability will be possible from current and future orbiting spacecraft using Doppler tracking data.

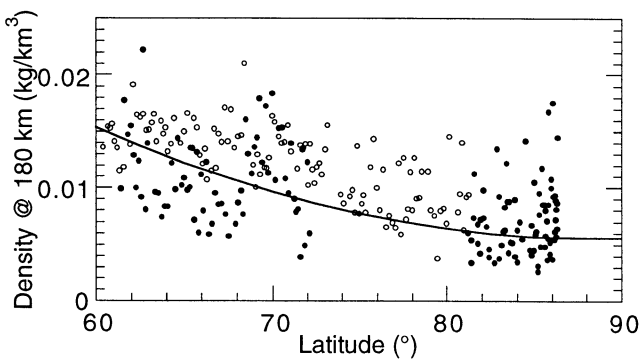

Figure 8. Density at 180 km versus latitude. Density scaling is the same as Figure 6. The solid circles are values from the first part of SPO (before L_S=0°), and the open circles are values from the second part of SPO. The general poleward slope is consistent with a high-latitude wind (polar "vortex") circulation pattern as modeled by *Bougher et al.* [2000] with the Mars Thermospheric Global Circulation Model (MTGCM). The line is model densities from *Bougher et al.* [2000, Figure 10a] MTGCM results with local time of 1500, southern summer solstice (L_S=270°), solar medium, "nondusty" conditions. See section 4.2 for discussion.

Acknowledgments. This work was performed as part of the Mars Global Surveyor Radio Science investigation with support from the NASA Mars Exploration program. We thank two reviewers for helpful comments and Dave Rowlands for GEODYN support.

References

Bougher, S.W., R.G. Roble, E.C. Ridley, and R.E. Dickinson, The Mars thermosphere, 2, General circulation with coupled dynamics and composition, *J. Geophys. Res.*, *95*(B9), 14,811-14,827, 1990.

Bougher, S.W., C.G. Fesen, E.C. Ridley, and R.W. Zurek, Mars mesosphere and thermosphere coupling: Semidiurnal tides, *J. Geophys. Res.*, *98*(E2), 3281-3295, 1993.

Bougher, S.W., S. Engel, R.G. Roble, and B. Foster, Comparative terrestrial planet thermospheres, 3, Solar cycle variation of global structure and winds at solstices, *J. Geophys. Res.*, *105*(E7), 17,669-17,692, 2000.

Boulton, W.J., The determination and analysis of the orbit of Nimbus 1 Rocket, 1964-52B – The semiannual variation in air density from June 1968 to August 1974, *Planet. Space Sci.*, *33*, 1417-1431, 1985.

Christensen, P.C., et al., Results from the Mars Global Surveyor Thermal Emission Spectrometer, *Science*, *279*, 1692-1698, 1998.

Clancy, R.T., B.J. Sandor, M.J. Wolff, P.R. Christensen, M.D. Smith, J.C. Pearl, B.J. Conrath, and R.J. Wilson, An intercomparison of ground-based millimeter, MGS TES, and Viking atmospheric temperature measurements: Seasonal and interannual variability of temperatures and dust loading in the global Mars atmosphere, *J. Geophys. Res.*, *105*(E4), 9553-9571, 2000.

Conrath, B.J., J.C. Pearl, M.D. Smith, W.C. Maguire, P.R. Christensen, S. Dason, and M.S. Kaelberer, Mars Global Surveyor Thermal Emission Spectrometer (TES) observations: Atmospheric temperatures during aerobraking and science phasing, *J. Geophys. Res.*, *105*(E4), 9509-9519, 2000.

Culp, R.D., and A.I. Stewart, Time-dependent model of the Martian atmosphere for use in orbit lifetime and sustenance studies, *J. Astronaut. Sci.*, *32*(3), 329-341, 1984.

Esposito, P., V. Alwar, S. Demcak, E. Graat, M. Johnston, and R. Mase, Mars Global Surveyor navigation and aerobraking at Mars, AAS Paper 98-384, in *AAS/GSFC International Symposium on Spaceflight Dynamics*, edited by T.H. Stengle, pp. 1015-1028, Univelt, San Diego, Ca., 1998.

Hinson, D.P., R.A. Simpson, J.D. Twicken, G.L. Tyler, and F.M. Flasar, Initial results from radio occultation measurements with Mars Global Surveyor, *J. Geophys. Res.*, *104*(E11), 26,997-27,012, 1999.

Justus, C.G., D.L. Johnson, and B.F. James, A revised thermosphere for the Mars Global Reference Atmospheric Model (Mars-GRAM Version 3.4), *NASA Tech. Memo.*, *NASA TM-1996-108513*, 1996.

Keating, G.M., et al., The structure of the upper atmosphere of Mars: In situ accelerometer measurements from Mars Global Surveyor, *Science*, *279*, 1672-1676, 1998.

Keating, G.M., R.H. Tolson, L.J. Ellis, M.S. Bradford, R.L. Stephens, D.T. Baird, S.W. Bougher, and J.L. Hollingsworth, First global mapping of the Mars thermosphere: MGS and MCO accelerometer experiment results, *Eos Trans. AGU*, *80*(46), Fall Meet. Suppl., F612-613, 1999.

Kieffer, H.H., T.Z. Martin, A.R. Peterfreund, B.M. Jakosky, E.D. Miner, and F.D. Palluconi, Thermal and albedo mapping of Mars during the Viking primary mission, *J. Geophys. Res.*, *82*, 4249-4291, 1977.

King-Hele, D., *Satellite Orbits in an Atmosphere: Theory and Applications*, 291 pp., Blackie, London, 1987.

Lemoine, F.G., The dynamics of orbiting satellites and gravity model development, Ph.D. thesis, Univ. of Colo. at Boulder, Boulder, Colo., 1992.

Lemoine, F.G., D.D. Rowlands, G.A. Neumann, D.E. Smith, D.E. Pavlis, D.S. Chinn, and S.B. Luthcke, Precise orbit determination for Mars Global Surveyor during hiatus and SPO, AAS Paper 99-147, in *Spaceflight Mechanics 1999*, edited by R.H. Bishop et al., pp. 649-666, Am. Astron. Soc., Washington, D. C., 1999a.

Lemoine, F.G., D.D. Rowlands, D.E. Smith, D.S. Chinn, D.E. Pavlis, S.B. Luthcke, G.A. Neumann, and M.T. Zuber, Orbit determination for Mars Global Surveyor during mapping, AAS Paper 99-328, in *Astrodynamics 1999: Proceedings of the AAS/AIAA Astrodynamics Conference Held August 16-19, 1999, Girdwood, Alaska*, edited by K.C. Howell et al., pp. 435-451, Univelt, San Diego, Ca., 1999b.

Lemoine, F.G., D.E. Smith, D.D. Rowlands, M.T. Zuber, G.A. Neumann, D.S. Chinn, and D.E. Pavlis, An improved solution of the gravity field of Mars (GMM-2B) from Mars Global Surveyor, *J. Geophys. Res.*, this issue.

Magalhães, J.A., J.T. Schofield, and A. Seiff, Results of the Mars Pathfinder atmospheric structure investigation, *J. Geophys. Res.*, *104*(E4), 8943-8955, 1999.

Moyer, T.D., Equations for computing programmed oscillator Doppler observables and partials in the ODP, *TM 391-412*, Jet Propul. Lab., Pasadena, Calif., Feb. 14, 1973.

Moyer, T.D., Changes to the ODP and the ODE for processing X-Band uplink data, *EM 314-430*, Jet Propul. Lab., Pasadena, Calif., Oct. 15, 1987.

Neumann, G.A., D.D. Rowlands, F.G. Lemoine, D.E. Smith, and M.T. Zuber, Crossover analysis of Mars Orbiter Laser Altimetric data, *J. Geophys. Res.*, this issue.

Nier, A.O., and M.B. McElroy, Composition and structure of Mars' upper atmosphere: Results from the neutral mass spectrometers on Viking 1 and 2, *J. Geophys. Res.*, *82*(28), 4341-4349, 1977.

Pavlis, D.E., S.G. Poulose, S.C. Rowton, and J.J. McCarthy, GEODYN operations manuals, Raytheon ITSS contractor report, Lanham, Md., April 9, 2001.

Seiff, A., and D.B. Kirk, Structure of the atmosphere of Mars in summer at mid-latitudes, *J. Geophys. Res.*, *82*(28), 4364-4378, 1977.

Smith, D.E., et al., The global topography of Mars and implications for surface evolution, *Science*, *284*, 1495-1503, 1999.

Smith, M.D., J.C. Pearl, B.J. Conrath, and P.R. Christensen, Mars Global Surveyor Thermal Emission Spectrometer (TES) observations of dust opacity during aerobraking and science phasing, *J. Geophys. Res.*, *105*(E4), 9539-9552, 2000.

Stewart, A.I.F., Revised time dependent model of the Martian atmosphere for use in lifetime and sustenance studies, *JPL PO NQ-802429*, Lab. for Atmos. and Space Phys., Univ. of Colo., Boulder, Colo., March 26, 1987.

Tolson, R.H., G.M. Keating, S.N. Noll, D.T. Baird, and T.J. Shellenberg, Utilization of Mars Global Surveyor accelerometer data for atmospheric modeling, AAS Paper 99-386, in *Astrodynamics 1999: Proceedings of the AAS/AIAA Astrodynamics Conference Held August 16-19, 1999, Girdwood, Alaska*, edited by K.C. Howell et al., pp. 1329-1338, Univelt, San Diego, Ca., 1999.

Tyler, G.L., G. Balmino, D.P. Hinson, W.L. Sjogren, D.E. Smith, R. Woo, S.W. Asmar, M.J. Connally, C.L. Hamilton, and R.A. Simpson, Radio science investigations with Mars Observer, *J. Geophys. Res.*, *97*, 7759-7779, 1992.

Walker, D.M.C., Cosmos 462 (1971-106A): Orbit determination and analysis, *Philos. Trans. R. Soc. London, Ser. A*, *292*(1396), 473-512, 1979.

Wilmoth, R.G., D.F. Rault, F.M. Cheatwood, W.C. Engelund, and R.W. Shane, Rarefied aerothermodynamic predictions for Mars Global Surveyor, *J. Spacecraft Rockets*, *36*(3), 314-322, 1999.

F. G. Lemoine and D. E. Smith, Laboratory for Terrestrial Physics, NASA Goddard Space Flight Center, Greenbelt, MD 20771, USA.

P. W. Tracadas and M. T. Zuber, Massachusetts Institute of Technology, 77 Massachusetts Avenue, Rm. 54-521, Cambridge, MA 02139, USA. (tracadas@mit.edu)

(Received October 24, 2000; revised May 25, 2001;
accepted June 5, 2001.)